Article:
Fu, X., Yin, L., Zhang, Y. et al. (5 more authors) (2025) SERS aptasensor detection of aflatoxin B1 based on silicon-au-ag Janus nanocomposites. Food Chemistry, 467. 142325. ISSN 0308-8146

https://doi.org/10.1016/j.foodchem.2024.142325

SERS aptasensor detection of Aflatoxin B1 based on silicon-Au-Ag Janus nanocomposites

Xuan Fu[a], Limei Yin[a, b], Yang Zhang[a], Ruiyun Zhou[a], Hesham R. El-Seedi[c,d], Xiaobo Zou[a,c], Yunyun Gong[b]*, Zhiming Guo[a, b]*

[a] *China Light Industry Key Laboratory of Food Intelligent Detection & Processing, School of Food and Biological Engineering, Jiangsu University, Zhenjiang 212013, China*

[b] *School of Food Science and Nutrition, University of Leeds, Leeds LS2 9JT, United Kingdom*

[c] *International Joint Research Laboratory of Intelligent Agriculture and Agri-products Processing, Jiangsu University, Zhenjiang 212013, China*

[d] *Department of Pharmaceutical Biosciences, Biomedical Centre, Uppsala University, Box 591, SE 751 24 Uppsala, Sweden*

*Corresponding author: School of Food and Biological Engineering, Jiangsu University, Zhenjiang 212013, China. Email addressed: guozhiming@ujs.edu.cn (Z. Guo), Y.Gong@leeds.ac.uk (Y. Gong)

ABSTRACT

Aflatoxin B1 (AFB1) is a prevalent contaminant in maize, posing significant threats to human health. This study designed Au-Ag Janus NPs with intrinsic Raman signals as signal probes and SiO_2@AgNPs as capture probes. The two were coupled through complementary base pairing to ensure the ordered, controlled distribution of noble metal nanoparticles. The Au-Ag Janus NPs and the highly stable SiO_2 carrier were performed to avoid the adverse effects on stability caused using signal molecules and the formation of random aggregates when using the noble metal nanoparticle gap effect to concentrate on the electromagnetic field. The negative impact of AgNPs high surface energy on their uniformity was improved, while enhancing the pH adaptability of Au-Ag Janus NPs. In the presence of AFB1, the composite disintegrates, and the SERS intensity showed a negative correlation with AFB1 concentration. enabled highly sensitive and stable detection of AFB1.

Keywords: Surface-enhanced Raman spectroscopy (SERS); Label-free; SiO_2; Au-Ag Janus NPs

1. Introduction

Maize, as the most extensively grown crop, is a vital raw material for both chemical and food industries, as well as a source of feed. However, mycotoxin contamination happens throughout the stages of maize growth, storage, and processing. Aflatoxin B1 (AFB1), a furano-coumarin compound generated by *Aspergillus flavus* and *A. parasiticus* (Zhang et al., 2024), is the most widely distributed, potent, and detrimental. It exhibits potent immunosuppressive, teratogenic, and carcinogenic effects (He et al., 2023; Li et al., 2023). Moreover, the maximum residue limit (MRL) of AFB1 in maize in China has been restricted to 20 μg/kg. Considering the significant threat, it poses to health of humanity and food security, the establishment of reliable AFB1 detection systems holds paramount importance. Conventional techniques for detecting AFB1 mainly involve enzyme-linked immunosorbent assay (ELISA) (Wu et al., 2020), liquid chromatography-mass spectrometry (LC-MS) (Chen et al., 2022), high-performance liquid chromatography (HPLC) (Jangampalli Adi & Matcha, 2018), thin-layer chromatography (TLC) (Amirkhizi et al., 2015). Due to their high accuracy and exceptional repeatability, these methods are extensively utilized. Nevertheless, they entail intricate sample preparation procedures, necessitate costly equipment and skilled personnel (Xue et al., 2024).

Surface-enhanced Raman scattering (SERS) is an emerging technology that relies on the optical enhancement phenomenon of localized surface plasmon resonance (LSPR) (Nanda et al., 2024). SERS techniques enable highly sensitive, swift, and quantitative detection with simple sample preparation procedures. Moreover, it has the

capability to gather data on molecular vibration and rotational energy levels, enabling it to achieve specific detection and greatly reducing the occurrence of false positive results (Pu et al., 2024; Wu et al., 2024). Therefore, SERS holds promising application prospects. The essence of SERS lies in the combination of Raman spectroscopy and an enhanced substrate (Goel et al., 2024). The composition, size, and surface morphology of the substrate are crucial factors that influence whether the SERS effect occurs and the strength of the SERS signal. "Hotspots" refer to areas on the surface of nanostructures where the local electromagnetic field is significantly enhanced, primarily based on LSPR. These regions are typically the places where the electromagnetic field enhancement is strongest on the SERS substrate (Li et al., 2024). Therefore, SERS substrates constructed based on the formation mechanism of "hotspots" can achieve excellent SERS enhancement effects.

Noble metal nanomaterials are currently the most extensively studied SERS enhancement substrates. Among them, Au and Ag nanomaterials are widely applied due to their advantages such as ease of preparation, significant enhancement effects, and the ability to achieve controllable localized surface plasmon resonance (LSPR) (Lv et al., 2024). In addition to the most common spherical structures, these materials can also be fabricated into different asymmetric anisotropic shapes using methods such as metal colloids and electrochemical etching (Ding & Zhu, 2015; Yang et al., 2017). Since the LSPR effect is stronger at the edges, such structures can effectively concentrate the electromagnetic field, creating stronger "hotspot" regions. Based on the edge enhancement effect, another "hotspot" formation mechanism is the nanoparticle gap

effect: when different metal nanoparticles come close to each other, forming many gaps with a certain distance, the local electromagnetic field is greatly enhanced in the narrow gaps between the particles (gap hotspots) (Duan et al., 2024). However, the distribution of pure Au, Ag nanoparticles in a colloidal state is easily influenced by the internal environment of the solution and is difficult to control. It may result in agglomerates where the spacing and arrangement of the nanoparticles are random, which can adversely affect the stability and reproducibility of the SERS signals.

To overcome the aforementioned issues, one approach could be to combine noble metal nanomaterials with other materials to improve their detection performance. Silicon dioxide (SiO_2) has well-developed preparation techniques that allow for effective control over its microstructure. Additionally, SiO_2 has a surface that is easy to chemically modify (Fu et al., 2024; Machado et al., 2024). Based on these characteristics, large-sized SiO_2 can serve as a carrier to allow small-sized noble metal nanoparticles to attach in an ordered and controlled manner, improving their uniformity and distribution density, thus better achieving "hotspot" enhancement effects. Compared to AuNPs, AgNPs exhibit more potent SERS enhancement effect, which is beneficial for highly sensitive SERS detection. However, the high surface energy of AgNPs may lead to excessive aggregation, low uniformity, thereby reducing the reproducibility of detection results (Granbohm et al., 2018). SiO_2, with its excellent stability and chemical inertness towards acidic and basic substances in the environment, can help improve the weaknesses of AgNPs when combined with them.

For mycotoxin with faint self-signals, these nanostructures often require additional

adsorption of Raman beacon molecules onto noble metal nanoparticles surface or embedding within the interstices of the core-shell structure to realize the detection of the target. This increases the risk of external interference, leading to comparatively fragile stability of SERS signals (Tan et al., 2024). Au-Ag Janus NPs can meet this requirement. These nanoparticles enable 2-mercapto-5-benzimidazole carboxylic acid (MBIA) usage as a ligand for surface modification of AuNPs, adjusting the Au-Ag interface energy, thereby inducing anisotropic growth of AgNPs to form Ag island structures following the Au core (Feng et al., 2015). Moreover, MBIA inherently displays Raman signals.

In this study, a SERS aptasensor based on SiO_2@AgNPs-Au-Ag Janus NPs for AFB1 detection was developed. The Au-Ag Janus NPs with intrinsic SERS signals can replace Raman signal molecules to generate signals, avoiding the adverse effects of prolonged contact between signal molecules and the noble metal enhancement substrate on stability. The high stability and acid-base resistance of SiO_2 are expected to further improve the stability of noble metal nanoparticles on the premise of promoting their controllable, uniform, and dense distribution as a carrier for small-sized noble metal nanoparticles, thereby enhancing the "hotspot" effect. Schematic illustration of the system was shown in Fig. 1. To the best of our knowledge, this is the first instance of using inert SiO_2 nanomaterials combined with gold-silver dimers for the specific detection of mycotoxins, proposing a new possibility for SERS sensors in protecting food safety.

2. Materials and methods

2.1 Materials and instruments

Silver nitrate ($AgNO_3$, ≥ 99%) and anhydrous ethanol (CH_3CH_2OH, ≥ 99.8%) were obtained from National Medicine Group Chemical Reagent Co., ltd (Shanghai, China). Polyvinylpyrrolidone (PVP, K30), chloroauric acid ($HAuCl_4 \cdot 4H_2O$, 99%), trisodium citrate ($C_6H_5Na_3O_7$, 98%) and tris (2-carboxyethyl) phosphine (TCEP, 98%) were acquired from McLean Biochemical Tech Co., Ltd (Shanghai, China). Ammonia water ($NH_3 \cdot H_2O$, 25-28%) was purchased from Hubao Chemical Reagents Co., ltd (Yangzhou, China). Tetraethyl orthosilicate (TEOS, 98%) was procured from Mairuier biochemical technology Co., ltd (Shanghai, China). 2-mercapto-5-benzimidazole carboxylic acid (MBIA, 97%) was bought from Bide Medicine Tech Co., ltd (Shanghai, China). Hydroquinone (HQ, ≥ 99%) was acquired from Aladdin biochemical Tech Co., Ltd (Shanghai, China). 4-mercaptobenzoic acid (4-MBA) was procured from Sigma-Aldrich (Shanghai, China). The standard aflatoxin B1 (AFB1) solution was purchased from Hua'an Magnech Bio-Tech Co., Ltd (Jinan, China). All materials and reagents utilized were of analytical grade, requiring no further purification. Throughout the entire experimental procedure, ultrapure water was employed. Thiol-functionalized AFB1 complementary aptamer (SH-cDNA) (5'-SH-CAG AGA GAC AAC ACG TGC CCA AC-3') and thiol-functionalized AFB1 aptamer (SH-apt) (5'-SH-GTT GGG CAC GTG TTG TCT CTC TGT GTC TCG TGC CCT TCG CTA GGC CC-3') were fabricated by Genscript Biotech Co., Ltd (Nanjing, China).

The morphology and structure of nanomaterials were analyzed by transmission electron microscopy (TEM, JEM-2100, JEOL, Akishima City, Tokyo, Japan). The ζ

potentials were obtained through particle size potentiometric analyzer (Anton Paar, Shanghai, China). UV-visible absorption spectra were collected using a UV-visible spectrophotometer (Anton Paar, Shanghai, China). X-ray diffraction (XRD, Rigaku, Tokyo, Japan) was utilized to examine the crystallographic structure of the nanoparticles. Fourier-transform infrared spectroscopy (FT-IR, Thermo Fisher, Waltham, USA) was utilized to obtain infrared spectra (Functional groups of the nanocomposite). A scanning transmission electron microscopy (STEM) equipped with an energy dispersive spectrometer (EDS) (STEM-EDS, JEOL, Akishima, Japan) and X-ray photoelectron spectroscopy (XPS, Shimadzu, Kyoto, Japan) were used for elemental analysis of nanomaterials. All Raman spectra were recorded using an automatic confocal micro-Raman imaging spectrometer (XploRA PLUS, HORIBA Scientific, Kyoto, Japan), and liquid chromatography was analyzed by a liquid chromatograph (Shimadzu LC-20AD, Shimadzu, Kyoto, Japan).

2.2 Synthesis of SiO_2@AgNPs

SiO_2 was prepared following the Stöber method (Stöber et al., 1968), with some adjustments. After uniform mixing ethanol (8 mL) with $NH_3 \cdot H_2O$ (3 mL), an ethanol (8 mL) and TEOS (2 mL) mixture solution was slowly dripped while stirring. The blend was agitated at room temperature (RT) for 24 h and then centrifuged (2260xg), washed six times with ethanol, and lastly, dried overnight in a vacuum environment at 60℃.

SiO_2@AgNPs were synthesized according to previous methods (Deng et al., 2007; Guo et al., 2023) with some modifications. A $[Ag(NH_3)_2]^+$ ion solution was prepared through the following steps. $NH_3 \cdot H_2O$ (5%, w/v) was slowly added dropwise into 4 mL

of $AgNO_3$ (0.4 M) solution with continuous shaking until the solution just became transparent, followed by dilution to a total volume of 12 mL with water. Then, SiO_2 (0.25 g) was dispersed in ethanol (10 mL). Subsequently, newly prepared $[Ag(NH_3)_2]^+$ ion solution (10 mL) was rapidly added, and the blend was continuously stirred at RT for 1 h. The mixture was centrifuged (1440xg) and washed six times with ethanol, then dried overnight under vacuum conditions at 60°C. The procedure for preparing standalone AgNPs solution was the same as the above steps excluding the addition of SiO_2 powder.

2.3 Synthesis of Au-Ag Janus NPs

AuNPs were synthesized using the sodium citrate reduction method (Zheng et al., 2019). First, 0.5 mL of $HAuCl_4 \cdot 4H_2O$ (1%, w/v) was introduced to water (49.5 mL) and heated until it reached a boil. Then, 1 mL of trisodium citrate (1%, w/v) was quickly added while stirring vigorously. and the mixture was continuously boiled until the color remained unchanged. Then, the previous mixture was cooled at RT.

The synthesis of Au-Ag Janus NPs was based on previous methods (Xu et al., 2023; Zhao et al., 2023) with several modifications. AuNPs (1 mL) was dissolved in water (9 mL), then mixed with MBIA (200 μL) and placed in a water bath at 60°C for 2h. While cooling to RT, 200 μL of HQ was introduced, and after the solution was uniformly mixed, different volumes (300, 600, 1200, 1800 μL) of $AgNO_3$ solution were added dropwise with vigorous stirring, slowly. The solution was obtained overnight at RT and then centrifuged (3250xg), and then re-dissolved in 2 mL water. The resulting nanoparticles were respectively named Au-Ag $Janus_{(1)}$ NPs, Au-Ag $Janus_{(2)}$ NPs, Au-

Ag Janus$_{(3)}$ NPs, and Au-Ag Janus$_{(4)}$ NPs.

2.4 DNA functionalization on SiO_2@AgNPs and Au-Ag Janus NPs

SH-cDNA and TCEP were mingled in a molar ratio of 1:100 and incubated at 37°C for 40 minutes to activate the thiol groups located at the end of cDNA (Chen et al., 2022). Then, 10 μL of activated SH-cDNA (100 μM) was further added into 1 mL of thoroughly sonicated SiO_2@AgNPs solution (1 mg/mL) and incubated for 12 h with shaking. After centrifugation (1260xg), the solution was resuspended in PBS buffer. The activation method for SH-apt was the same as for activating SH-cDNA. Afterward, 5 μL of activated SH-apt (100 μM) was introduced into Au-Ag Janus NPs (1 mL) and incubated with agitation for 12 h. The solution was then centrifuged (2950xg) and reconstituted in PBS buffer.

2.5 Establishment of SERS aptasensor for AFB1 detection

The capture probe (SiO_2@AgNPs-cDNA) and signal probe (Au-Ag Janus NPs-apt) were blended and incubated at varying volume ratios to assemble the SERS aptasensor (SiO_2@AgNPs-cDNA-apt-Au-Ag Janus NPs). The capture probe with 100 μL was mixed separately with 100, 200, 300, 400 and 500 μL of signal probe, and shaken at 37°C for 2 h. The solution underwent centrifugation (560xg), and the sediment was resuspended in 100 μL of PBS buffer. The ultimate solution was then stored at 4°C.

The AFB1 standard solutions, each totaling 100 μL and varying in concentration (0.0001, 0.001, 0.01, 0.1, 1, 10, 50, 100 ng/mL), underwent a 2-hour incubation period with an equal volume of SERS aptasensor to capture AFB1, and the complex was

centrifuged (360xg) to eliminate free signal probes. Later, the product was suspended again in 100 μL of PBS buffer solution. A laser confocal Raman microscope equipped with a 638 nm excitation wavelength and a 10 × objective was used to collect the Raman spectra of the assemblies. The spectral range extended from 400 to 2000 cm^{-1}, with an integration time of 10 s. The Raman intensity of MBIA at 1280 cm^{-1} was collected five times for each sample, and the average value was used for the quantitative analysis of AFB1. Additionally, for stability (3.2) or reproducibility (3.6) assessment, the scanning area was 120 × 120 μm.

The Raman characteristic peaks used for 4-MBA and MBIA were 1589 and 1280 cm^{-1}, respectively, and quantitative analysis of AFB1 concentration was performed based on the intensity of the MBIA characteristic peak, with 5 spectral data collected for each sample. Additionally, unless otherwise specified, the scanning area for simultaneously and randomly collecting 30 or more spectra was 120 × 120 μm.

2.6 Specificity evaluation of aptasensor

To assess the specificity of the aptasensor, other toxins commonly found in maize (ZEN, FB1, OTA, DON) at a concentration of 10 ng/mL were chosen as interferents. They were incubated with the aptasensor established under optimal conditions using the same method as for AFB1 (0.1 ng/mL). Changes in SERS intensity were then compared.

2.7 Maize meal and oil sample detection and specificity analysis

To validate the practical applicability of the aptasensor for detecting AFB1, positive maize meal naturally contaminated with AFB1, or artificially spiked maize

meal and maize oil with AFB1 standard solution, were used as detection samples. The sample pretreatment process followed the HPLC-post-column derivatization method in the National Standard of China (GB 5009.22-2016) with minor modifications.

Equal volumes of gradient concentration AFB1 standard solution were added to 1 g of maize meal to simulate contaminated maize tissue (this step was not required for the naturally contaminated maize meal). The samples stood at RT for 2 h, then 10 mL of methanol (70%, w/v) and 0.4 g of NaCl were introduced. They were vortexed for 20 minutes, subsequently centrifuged (3822xg) for 10 minutes. The resulting supernatant could be used for SERS detection, while further purification was required for HPLC detection. The supernatant, 10 mL in volume, was blended with 30 mL of water and filtered through glass fiber filter paper to remove impurities. Then, 40 mL of the filtrate slowly passed through an immunoaffinity column until no droplets dripped down. The immunoaffinity column was rinsed with 2 × 10 mL of water, and a rolled-up fast quantitative filter paper strip was inserted into the column wall and gently rotated to absorb moisture. All the above solutions were discarded. AFB1 adsorbed on the inner wall of the immunoaffinity column was eluted with methanol (1 mL), and the eluate was passed through a membrane (0.22 μm) for HPLC detection. The maize oil samples underwent the same pretreatment method as the maize meal.

HPLC with a fluorescence detector was employed for the analysis. Here are the chromatographic conditions: C18 column (150 × 4.6 mm × 3 μm), column temperature: 40℃, incoming sample volume: 20 μL, flow rate: 0.8 mL/min, mobile phase: methanol:water (1/1, v/v), excitation wavelength: 360 nm, emission wavelength: 440

nm.

ZEN, FB1, OTA, and DON were used as interferents to prepare 1 g spiked maize meal/oil samples. After pre-treatment, samples containing ZEN (100 μg/kg), FB1 (100 μg/kg), OTA (100 μg/kg), DON (100 μg/kg) and AFB1 (10 μg/kg) were detected to further evaluate the selectivity of the aptasensor for AFB1 in maize samples.

3. Results and discussion

3.1 Construction of a SERS platform for specific Detection of AFB1

The fabrication of the SERS aptasensor is described in Fig. 1. A newly prepared $[Ag(NH_3)_2]^+$ ion solution was introduced to the SiO_2 using the Stöber method. Because of the negatively charged silanol groups, $[Ag(NH_3)_2]^+$ ions easily adhered to the surface of the SiO_2 nanospheres through electrostatic interactions. Then, PVP was introduced to reduce the $[Ag(NH_3)_2]^+$ ions, synthesizing SiO_2@AgNPs and stabilizing the AgNPs. With MBIA as the ligand and HQ as the reducing agent, Ag islands were guided to grow on AuNPs synthesized by the sodium citrate method. The resulting Au-Ag Janus NPs exhibited intrinsic SERS signals. SiO_2@AgNPs and Au-Ag Janus NPs were respectively modified with Apt_{AFB1}-C and Apt_{AFB1}. Under optimal conditions, assemblies were formed based on complementary base pairing, showing enhanced SERS signals. With AFB1 present, Apt_{AFB1} preferentially bound to it, causing the Au-Ag Janus NPs to detach from SiO_2@AgNPs and the signal to decrease, thereby enabling the construction of a competitive SERS aptasensor for detecting AFB1.

3.2 Characterization of SiO_2@AgNPs-cDNA

The microstructure and physical appearance of SiO_2 and SiO_2@AgNPs are shown

in Fig. 2A-C. SiO_2 appeared as spherical particles with a size of approximately 753 nm. The nearly spherical AgNPs, with the size of 62 nm, were uniformly and densely dispersed on the surface of SiO_2, demonstrating the role of SiO_2 as a carrier for AgNPs. Additionally, according to the physical images, SiO_2 turned from white to brown powder when combined with AgNPs. XRD spectrum (Fig. 2D) demonstrates that the SiO_2 in has one amorphous diffraction peak with 2θ at 24°. SiO_2@AgNPs showed new diffraction peaks at 38.15°, 44.26°, 64.48°, and 77.52°, corresponding to the (111), (200), (220), (311) crystal phases of silver, which indicates the formation of AgNPs with crystal-linity. Additionally, the comparison of FT-IR spectra between SiO_2 and SiO_2@AgNPs is depicted in Fig. 2E. Absorption bands around 793 and 1050 cm^{-1} correspond to the symmetric and asymmetric Si-O-Si stretching vibrations, respectively. The absorption at 949 cm^{-1} was attributed to the bending vibration of Si-OH, while the bending and stretching vibration of -OH appeared at 1610 and 3383 cm^{-1}. Combined with locally amplified spectra, the -OH-related absorption peak of SiO_2@AgNPs was weaker than that of SiO_2, which may be due to the reduction in the -OH content on the surface of SiO_2 after being capped by PVP (Li et al., 2021). According to the XPS characterization of SiO_2@AgNPs (Fig. 2F and Fig. S1), the appearance of characteristic peaks for C 1s and N 1s further indicated the existence of PVP on the surface of SiO_2@AgNPs, while the presence of characteristic peaks for O 1s, Si 2p, and Ag 3d confirmed the existence of silicon, oxygen, and silver materials in SiO_2@AgNPs, respectively. The XPS analysis of Ag 3d revealed two peaks situated at 368.2 and 374.2 eV, with a spin-orbit separation of 6 eV, corresponding to Ag $3d_{5/2}$ and Ag $3d_{3/2}$ binding

296 energies, confirming the presence of zero-valent Ag (Niu et al., 2015). The above
297 characterizations provide reliable evidence for the successful preparation of
298 SiO_2@AgNPs.

299 SiO_2 displayed no apparent UV-vis absorption peak, whereas SiO_2@AgNPs
300 exhibited an absorption peak at 408 nm, attributed to AgNPs, following incubation with
301 Apt_{AFB1}-C, a new peak emerged at 264 nm, denoting successful coupling between the
302 nanoparticles and Apt_{AFB1}-C (Fig. 2G). Better physical stability is achieved with higher
303 absolute values of the ζ potential, which increase electrostatic repulsion between
304 particles (Kriegseis et al., 2020). As depicted in Fig. 2H, the mean potential of AgNPs
305 was -18.46 mV, and that of SiO_2 was -66.2 mV, indicating a very high absolute value,
306 which is consistent with its excellent stability. The mean absolute value of the
307 composite's potential slightly decreased (-60.78 mV), but the value remained high,
308 confirming the improvement in the stability of AgNPs by SiO_2. The individual raw
309 concentration AgNPs and SiO_2@AgNPs (1 mg/mL) were respectively incubated with
310 4-MBA (4.5×10^{-4} M) for 40 minutes, then, 30 peak values at 1589 cm^{-1} of the beacon
311 molecules were randomly collected for both. AgNPs exhibited an RSD of 20.40%,
312 whereas SiO_2@AgNPs displayed a lower RSD of 8.16% (Fig. S2A-B), demonstrating
313 improved uniformity. This improvement in the uniformity of AgNPs by SiO_2 was
314 further supported by the particle size distribution diagrams of AgNPs, SiO_2, and
315 SiO_2@AgNPs (Fig. S2C-E). As shown in Fig. 2I, SiO_2 did not exhibit any discernible
316 SERS enhancement. AgNPs combined with SiO_2 showed signal intensity comparable
317 to that of higher-concentration standalone AgNPs, even at relatively low concentrations.

This improvement is likely attributed to the dense arrangement of AgNPs, which promotes the generation of hotspots.

3.3 Characterization of Au-Ag Janus NPs-apt

The prepared AuNPs were uniformly dispersed in solution and appeared purple-red (Fig. 3A). The mean diameter of the Au nanoparticles was 38.96 nm (Fig. S5A). By adding 60 μL of $AgNO_3$, Ag islands grew on the sides of the AuNPs, resulting in Au-Ag Janus NPs, which exhibited a unique anisotropic structure and turned brown-yellow (Fig. 3B). The Ag islands of the Au-Ag Janus NPs had an approximate particle size of 42.20 nm (Fig. 3C). The AuNPs displayed a strong UV-vis absorption peak at 526 nm. For Au-Ag Janus NPs, two peaks at 400 nm and 800 nm were observed corresponding to the transverse absorption of AgNPs and the longitudinal absorption of Au-Ag Janus NPs, respectively (Feng et al., 2017). Meanwhile, the absorption peak of AuNPs blue-shifted to 513 nm (Fig. 3D). The ζ potential of Au-MBIA was -33.12 mV, which decreased to -22.76 mV for the Au-Ag Janus NPs, consistent with previous reports (Wang et al., 2022). The negative potential increased (-25.91 mV) after the nanoparticles were coupled with Apt_{AFB1}, attributed to the negative charges provided by the phosphate groups in the aptamer (Fig. 3E) (Wu et al., 2024). STEM-element content examination was used to assess the composition distribution of Au-Ag Janus NPs, showing that they were primarily composed of Au and Ag elements, confirming the presence of both the Au core and Ag islands (Fig. S3A). Additionally, EDS line scan profiles further demonstrated the formation of Ag islands on the sides of the AuNPs (Fig. S3B).

The SERS intensity was continuously and randomly collected at 36 points on the Au-Ag Janus NPs. Their SERS spectra showed good consistency (Fig. S6A-B), with a peak RSD of 4.53% at 1280 cm^{-1} (Fig. 3F), demonstrating excellent reproducibility. To explore the stability of Au-Ag Janus NPs as signal probes, their SERS signal was investigated under different pH values (6, 6.5, 7, 8, 9, 10, 11), temperatures (20, 35, 45, 60°C), and storage times (0, 7, 14 days). Within the pH range of 7-11, the nanoparticles exhibited similar signal intensities at 1280 cm^{-1}, and the solution remained uniform and stable. When the pH was 6.5, the system underwent aggregation, and exhibited a significant decrease in signal intensity, which further decreased as the pH value was lowered (Fig. 3G). This illustrated that Au-Ag Janus NPs had excellent stability under neutral and alkaline conditions. The SERS intensity of Au-Ag Janus NPs showed no significant changes under different temperatures or storage times (Fig. 3H), proving their good environmental adaptability.

Au-Ag Janus NPs featuring varying Ag island dimensions were synthesized using different volumes of 300, 600, 900, and 1200 μL for $AgNO_3$ solution, respectively, resulting in Au-Ag $Janus_{(1)}$ NPs, Au-Ag $Janus_{(2)}$ NPs, Au-Ag $Janus_{(3)}$ NPs, and Au-Ag $Janus_{(4)}$ NPs (Fig. 3B and Fig. S4). The approximate particle sizes of the Ag islands were 30.56, 42.20, 52.65, and 80.62 nm (Fig. 3C and Fig. S5B-D). The SERS signal intensity of the Au-Ag Janus NPs at 1280 cm^{-1} is shown in Fig. 3I. As the dimensions of the Ag islands grew, the signal initially increased. The highest SERS signal was obtained with Au-Ag $Janus_{(2)}$ NPs. Additionally, excessively large Ag islands caused the dimeric nanoparticle structures to become irregular, leading to a decrease in signal

reproducibility and stability. Therefore, 600 μL was chosen as the optimal amount of $AgNO_3$.

3.4 Optimization of SERS aptasensor and stability assessment

The TEM characterization of the SERS aptasensor is depicted in Fig. 4A-B. The surface of SiO_2@AgNPs was covered with Au-Ag Janus NPs. The STEM elemental mapping (Fig. 4C-D) indicated the presence of Si, O, Ag, and Au elements, further verifying the formation of SiO_2@AgNPs-Au-Ag Janus NPs assemblies. As seen in Fig. 4E, the assemblies maintained the UV-vis absorption peak characteristic of Au-Ag Janus NPs, with an enhanced peak for AgNPs and a weakened peak for AuNPs. This is due to the high content of AgNPs in aptasensor, and relative low content of the AuNPs. This explanation is further corroborated by comparing the STEM elemental content analysis of Ag-Ag Janus NPs (Fig. S3A) and the SERS aptasensor (Fig. S7A). SiO_2@AgNPs themselves did not exhibit obvious SERS signals, while Au-Ag Janus NPs displayed inherent signals. The assemblies showed a significant SERS enhancement effect (Fig. 4F).

The stability of the SERS aptasensor was confirmed by collecting SERS signals after placing them in various environments with different pH values and temperatures; and storing them for different storage times. As shown in Fig. 4G, compared to the Au-Ag Janus NPs, the composites exhibited similar signal intensities in the pH range of 4-11 and maintained stability at different temperatures and storage times. This improvement addresses the weakness of Au-Ag Janus NPs' poor stability under acidic conditions, resulting in a system with excellent stability.

The optimal ratio of capturing probes to signal probes was determined by mixing and incubating them in varying volume ratios (1:1, 1:2, 1:3, 1:4, 1:5), followed by Raman detection. As shown in Fig. 5A, as the ratio of the two probes increased from 1:1 to 1:4, the SERS signal intensity of the system gradually increased and reached its maximum. This is explained by the fact that the 1:4 ratio achieved the saturation binding number of Au-Ag Janus NPs on SiO_2@AgNPs. When more Au-Ag Janus NPs were added, no further coupling occurred. Therefore, 1:4 was chosen as the optimal binding ratio. To detect AFB1 efficiently, the duration of incubation of the SERS aptasensor with AFB1 was optimized (Fig. 5B). As the incubation time increased, the system's signal intensity gradually decreased, which stemmed from the high specific affinity of Apt_{AFB1} for AFB1 leading to the decrease of Au-Ag Janus NPs on SiO_2@AgNPs. The SERS signal intensity stabilized and reached its minimum after an incubation time of 2 h. Therefore, Thus, the ideal reaction duration was established as 2 h.

3.5 Application of SERS aptasensor in AFB1 detection

To validate the analytical performance of the SERS aptasensor, multiple SERS responses were acquired by incubating the established sensor with AFB1 concentrations varying from 0.0001 to 100 ng/mL. The SERS intensity decreased with increasing AFB1 concentration, showing a negative correlation in line with the competitive principle of the system (Fig. 5C). Through plotting the logarithmic values of AFB1 concentration against the intensity of the 1280 cm^{-1} peak values of MBIA, a standard curve was established, revealing a good linear relationship within the concentration range of 0.001 to 100 ng/mL of AFB1 (Fig. 5D). The equation of linear regression was

found to be y = -3286.44 ± 146.61x + 11927.26 ± 209.89 with the correlation coefficient (R^2) of 0.990. The limit of detection (LOD) was calculated based on the signal-to-noise ratio (SNR) of 3 and the value is 0.5 pg/mL. Furthermore, compared to previously reported SERS methods for AFB1 analysis, this platform demonstrated a broader linear detection range and a reduced LOD (Table 1A).

3.6 Evaluation of specificity and reproducibility for AFB1 analysis

The fabricated SERS aptasensor was employed for the detection of 10 ng/mL of ZEN, FB1, OTA, and DON, as well as 0.1 ng/mL of AFB1 (Fig.5E). Even when the concentration of other toxins was 100 times that of AFB1, the signal intensity was nearly equal to that of the blank group, while the presence of AFB1 caused a significant decrease in SERS intensity. This outcome indicates that SERS aptasensor exhibits excellent recognition selectivity for AFB1.

Reproducibility is another crucial factor for assessing the system's quality. 36 points were continuously measured with the SERS aptasensor capturing 50 ng/mL of AFB1. The Raman characteristic peaks of MBIA exhibited similar intensities (Fig. S7B), and the RSD value of the signal intensity at 1280 cm^{-1} was 5.97% (Fig. 5F), indicating the great reproducibility of the composite system.

3.7 AFB1 analysis in maize meal and maize oil and specificity analysis

The practicality of the SERS aptasensor was validated by incorporating it into the detection of maize samples. Naturally contaminated maize meal, spiked maize meal and maize oil were used as detection samples, and the initial AFB1 concentrations in the spiked maize meal and oil verified as 0 ng/mL via HPLC (Fig. S10A-B). The AFB1

concentration in the samples was calculated with the measured signal intensity and the assistance of the established standard curve. The formula is as follows:

$$X = \frac{\rho \times V}{m} \quad (1)$$

X —— the content of AFB1 in the sample (μg/kg)

ρ —— the concentration of AFB1 in the sample solution calculated from the standard curve (ng/mL)

V —— final volume (mL)

m —— sample weight (g)

To validate the accuracy of this SERS platform, the detection results were compared with those obtained by HPLC method. The SERS spectra for the representative samples are illustrated in Fig. S8. The standard HPLC curve and representative samples' chromatograms are presented in Fig. S9 and Fig. S10C-H, respectively. SERS and HPLC detection methods respectively exhibited negative and positive correlations with the concentration of AFB1, consistent with the theoretical expectations. In Table 1B, the SERS aptasensor detection exhibited a recovery rate ranging from 114.04 to 88.70%, with an RSD (n = 5) between 0.58% and 1.56%. Moreover, the Tukey t-test indicated that there is no significant difference between the proposed SERS and the traditional HPLC detection method ($P > 0.05$). This demonstrates that the system shows the anticipated accuracy and holds great potential for practical applications.

In the maize samples, whether in meal or oil form, only the presence of AFB1 caused a significant decrease in the SERS intensity of the aptasensor (Fig. S11),

indicating that the system also exhibits good selectivity for AFB1 in complex matrices.

4.Conclusion

In summary, a label-free SERS aptasensor based on SiO_2@AgNPs-Au-Ag Janus NPs was developed to detect and analyze AFB1. The integration of AgNPs with the extensive surface area of SiO_2, enhanced their stability and created densely packed hotspots. Undoubtedly, MBIA played a key role in the synthesis of Au-Ag Janus NPs, boosting the SERS signal as a substitute for Raman beacon molecules as well as avoiding the negative impact of beacon molecules on the stability of the nanoparticles. Ultimately, through the induction of the Apt_{AFB1}-C and Apt_{AFB1}, the two assembled into a highly stable SERS probe with a strong signal. The occurrence of AFB1 led to disintegration of the components, resulting in a decrease in signal intensity. This SERS aptasensor exhibited a broad linear detection range (0.001-100 ng/mL) and a low LOD (0.5 pg/mL), as well as satisfactory specificity and reproducibility. In the analysis of actual samples, the system effectively detected AFB1 in both naturally contaminated and spiked maize meal, and oil, with a recovery rate ranging from 114.04 to 88.70%, and results comparable to those obtained with the national standard HPLC method. Therefore, this system demonstrates excellent sensitivity and accuracy, showing great potential for practical applications. Nonetheless, in actual samples, maize is often simultaneously contaminated with multiple mycotoxins. Therefore, achieving simultaneous detection of multiple toxins is an area that we plan to explore and improve in the future. This could potentially be accomplished by using aptamers for various toxins and exploring stable signal sources with Raman peaks that do not overlap with

the MBIA Raman characteristic peak.

Acknowledgements

This research was funded by the National Natural Science Foundation of China (32472431, 32301690, 32350410403), China Scholarship Council (202208690011), the Natural Science Foundation of Jiangsu Province (BK20210748) and Advanced Talents Science Foundation of Jiangsu University (21JDG055).

References

Amirkhizi, B., Arefhosseini, S. R., Ansarin, M., & Nemati, M. (2015). Aflatoxin B1 in eggs and chicken livers by dispersive liquid-liquid microextraction and HPLC. *Food Additives Contaminants: Part B: Surveillance*, *8*(4), 245-249. https://doi.org/10.1080/19393210.2015.1067649

Cao, H., Liang, D., Tang, K., Sun, Y., Xu, Y., Miao, M., & Zhao, Y. (2024). SERS and MRS signals engineered dual-mode aptasensor for simultaneous distinguishment of aflatoxin subtypes. *Journal of Hazardous Materials*, *462*, 132810. https://doi.org/https://doi.org/10.1016/j.jhazmat.2023.132810

Chen, M., Liu, X., Yang, S., Chen, Z., Di, B., Liu, W., & Yan, H. (2022). HPLC–MS/MS method for the simultaneous determination of aflatoxins in blood: toxicokinetics of aflatoxin B1 and aflatoxin M1 in rats. *Journal of Analytical Science and Technology*, *13*(1). https://doi.org/10.1186/s40543-022-00336-3

Chen, P., Li, C., Ma, X., Wang, Z., & Zhang, Y. (2022). A surface-enhanced Raman scattering aptasensor for ratiometric detection of aflatoxin B1 based on graphene oxide-Au@Ag core-shell nanoparticles complex. *Food Control*, *134*, 108748. https://doi.org/10.1016/j.foodcont.2021.108748

Deng, Z. W., Chen, M., & Wu, L. M. (2007). Novel method to fabricate SiO_2/Ag composite spheres and their catalytic, surface-enhanced Raman scattering properties [Article]. *Journal of Physical Chemistry C*, *111*(31), 11692-11698. https://doi.org/10.1021/jp073632h

Ding, S.J., & Zhu, J. (2015). Tuning the surface enhanced Raman scattering activity of gold nanocubes by silver coating. *Applied Surface Science*, *357*, 487-492. https://doi.org/10.1016/j.apsusc.2015.09.077

Duan, L., Liu, X., Meng, X., & Qu, L. (2024). Highly sensitive SERS detection of pesticide residues based on multi-hotspot buckypaper modified with gold nanoparticles. *Spectrochimica Acta Part A: Molecular and Biomolecular Spectroscopy*, *308*, 123665. https://doi.org/https://doi.org/10.1016/j.saa.2023.123665

Feng, Y., Wang, Y., He, J., Song, X., Tay, Y. Y., Hng, H. H., Ling, X. Y., & Chen, H. (2015). Achieving Site-Specificity in Multistep Colloidal Synthesis. *Journal of the American Chemical Society*, *137*(24), 7624-7627. https://doi.org/10.1021/jacs.5b04310

Feng, Y., Wang, Y., Song, X., Xing, S., & Chen, H. (2017). Depletion sphere: Explaining the number of Ag islands on Au nanoparticles. *Chemical Science*, *8*(1), 430-436. https://doi.org/10.1039/c6sc02276f

Fu, L., Zhou, Z., Zheng, Y., Dong, B., & Chen, S. (2024). Hydrophobic SiO_2 in anti-fouling building application. *Construction and Building Materials*, *448*, 138232. https://doi.org/https://doi.org/10.1016/j.conbuildmat.2024.138232

Goel, R., Chakraborty, S., Awasthi, V., Bhardwaj, V., & Kumar Dubey, S. (2024). Exploring the various aspects of Surface enhanced Raman spectroscopy (SERS) with focus on the recent progress: SERS-active substrate, SERS-instrumentation, SERS-application. *Sensors and Actuators A: Physical*, *376*, 115555. https://doi.org/https://doi.org/10.1016/j.sna.2024.115555

Granbohm, H., Larismaa, J., Ali, S., Johansson, L. S., & Hannula, S. P. (2018). Control of the Size of Silver Nanoparticles and Release of Silver in Heat Treated SiO_2-Ag Composite Powders. *Materials (Basel)*, *11*(1). https://doi.org/10.3390/ma11010080

Guo, H., Ren, X., Song, X., & Li, X. (2023). Preparation of SiO_2@Ag@molecular imprinted polymers hybrid for sensitive and selective detection of amoxicillin using surface-enhanced Raman scattering. *Spectrochimica Acta part A Molecular and Biomolecular Spectroscopy*, *291*, 122365. https://doi.org/10.1016/j.saa.2023.122365

Guo, Z. M., Fu, X., Zhou, R. Y., Zhang, Y., El-Seedi, H., Watson, N., Zou, X. B., & Povey, M. (2024). A silicon-based functional self-assembled aptasensor for the detection of aflatoxin B1 by SERS sensing. *Analutical Methods*, *16*(41), 6994-7004. https://doi.org/10.1039/d4ay01266f

He, H., Sun, D. W., Pu, H., & Wu, Z. (2023). A SERS-Fluorescence dual-signal

aptasensor for sensitive and robust determination of AFB1 in nut samples based on Apt-Cy5 and MNP@Ag-PEI. *Talanta*, *253*, 123962. https://doi.org/10.1016/j.talanta.2022.123962

Jangampalli Adi, P., & Matcha, B. (2018). Analysis of aflatoxin B1 in contaminated feed, media, and serum samples of Cyprinus carpio L. by high-performance liquid chromatography. *Food Quality and Safety*, *2*, 199-204 https://doi.org/10.1093/fqsafe/fyy013

Jiao, T., Dong, C., Zhu, A., Ahmad, W., Peng, L., Wu, X., Chen, Q., Wei, J., Chen, X., Qin, O., & Chen, Q. (2025). AFB1-responsive mesoporous silica nanoparticles for AFB1 quantification based on aptamer-regulated release of SERS reporter. *Food Chemistry*, *463*, 141417. https://doi.org/https://doi.org/10.1016/j.foodchem.2024.141417

Kriegseis, S., Vogl, A. Y., Aretz, L., Tonnesen, T., & Telle, R. (2020). Zeta potential and long-term stability correlation of carbon-based suspensions for material jetting. *Open Ceramics*, *4*, 100037. https://doi.org/https://doi.org/10.1016/j.oceram.2020.100037

Li, J., Xu, Y., Tian, L., Yan, Y., Niu, L., Li, X., & Zhang, Z. (2021). Silver Nanoparticle-Decorated Silica Nanospheres and Arrays as Potential Substrates for Surface-Enhanced Raman Scattering. *ACS Omega*, *6*(48), 32879-32887. https://doi.org/10.1021/acsomega.1c04874

Li, K., Tang, X., Wang, H., Huang, M., Liu, G., Zhou, Y., Huang, W., & Zuo, Z. (2024). Large-area Ag “sesame cake-like” arrays with high-density hotspots for efficient SERS analysis. *Applied Surface Science*, *669*, 160544. https://doi.org/https://doi.org/10.1016/j.apsusc.2024.160544

Li, X., Meng, F., Li, Z., Li, R., Zhang, Y., & Zhang, M. (2023). Dual-signal aptasensor based on Zr-MOF for ultrasensitive detection of AFB1 in corn. *Sensors and Actuators B: Chemical*, *394*, 134372. https://doi.org/10.1016/j.snb.2023.134372

Lv, J., Wang, G., Li, Y., Li, Z., Yu, Y., Wang, Y., & Lv, Z. (2024). Status and applications

565 of femtosecond laser preparation of SERS substrates containing noble metals
566 nanoparticles. *Surfaces and Interfaces*, *51*, 104719.
567 https://doi.org/https://doi.org/10.1016/j.surfin.2024.104719
568 Machado, Y. D. R., Germano, G. C. M., Pecoraro, E., Costa, A. M. L. M., & Carvalho,
569 I. C. S. (2024). Impact of SiO_2 nanoparticle morphology on scattering efficiency
570 for random lasers. *Optical Materials*, *148*, 114775.
571 https://doi.org/https://doi.org/10.1016/j.optmat.2023.114775
572 Nanda, B. P., Rani, P., Paul, P., Aman, Subrahmanya S, G., & Bhatia, R. (2024). Recent
573 Trends and Impact of Localized Surface Plasmon Resonance (LSPR) and
574 Surface-Enhanced Raman Spectroscopy (SERS) in Modern Analysis. *Journal*
575 *of Pharmaceutical Analysis*. https://doi.org/10.1016/j.jpha.2024.02.013
576 Niu, P., Liu, B., Li, Y., Wang, Q., Dong, A., Hou, H., Zhang, L., Gao, Y., & Zhang, J.
577 (2015). CdTe@SiO_2/Ag nanocomposites as antibacterial fluorescent markers
578 for enhanced latent fingerprint detection. *Dyes and Pigments*, *119*, 1-11.
579 https://doi.org/10.1016/j.dyepig.2015.03.018
580 Pu, H., Ouyang, Q., & Sun, D.-W. (2024). Special chemical reactions combined with
581 SERS techniques for improving detection of trace and Raman-inactive food
582 contaminants: Principles and applications. *Trends in Food Science &*
583 *Technology*, *147*, 104416. https://doi.org/10.1016/j.tifs.2024.104416
584 Stöber, W., Fink, A., & Bohn, E. (1968). Controlled growth of monodisperse silica
585 spheres in the micron size range. *Journal of Colloid and Interface Science*, *26*(1),
586 62-69. https://doi.org/https://doi.org/10.1016/0021-9797(68)90272-5
587 Tan, X., Kang, K., Zhang, R., Dong, J., Wang, W., & Kang, W. (2024). An ultrasensitive
588 dual-mode approach for AFB1 detection: Colorimetric/label-free SERS
589 aptasensor based on a self-assembled core-shell structured Ag@Au IP6
590 bifunctional nanozyme. *Sensors and Actuators B: Chemical*, *412*, 135854.
591 https://doi.org/10.1016/j.snb.2024.135854
592 Wang, J., Luo, D., Cai, Y., Li, X. L., Chen, H. Y., & Xu, J. J. (2022). A plasmonic Au-
593 Ag janus nanoprobe for monitoring endogenous hydrogen sulfide generation in

living cells. *Biosensors Bioelectronics*, *213*, 114422. https://doi.org/10.1016/j.bios.2022.114422

Wu, F., Chen, G., Lai, K., Zhang, S., Liu, Y., Luo, R., Wang, X., Cao, P., Ye, Y., Lian, J., Qu, J., Yang, Z., & Peng, X. (2024). Non-specific/specific SERS spectra concatenation for precise bacteria classifications with few samples using a residual neural network. *Chinese Chemical Letters*, 109884. https://doi.org/10.1016/j.cclet.2024.109884

Wu, L., Zhou, M., Wang, Y., & Liu, J. (2020). Nanozyme and aptamer- based immunosorbent assay for aflatoxin B1. *Journal of Hazardous Materials*, *399*, 123154. https://doi.org/10.1016/j.jhazmat.2020.123154

Wu, X., Yin, L., Gao, S., Zhou, R., Zhang, Y., Xue, S., Jayan, H., El-Seedi, H. R., Zou, X., & Guo, Z. (2024). Core-satellite nanoassembly system with aptamer-conjugated Au@Ag nanoparticles for SERS detection of patulin in apples. *Food Control*, *159*, 110293. https://doi.org/https://doi.org/10.1016/j.foodcont.2024.110293

Wu, Z., Sun, D. W., Pu, H., Wei, Q., & Lin, X. (2022). Ti_3C_2Tx MXenes loaded with Au nanoparticle dimers as a surface-enhanced Raman scattering aptasensor for AFB1 detection. *Food Chemistry*, *372*, 131293. https://doi.org/https://doi.org/10.1016/j.foodchem.2021.131293

Xu, Y., Jin, Z., & Zhao, Y. (2023). Tunable Preparation of SERS-Active Au–Ag Janus@Au NPs for Label-Free Staphylococcal Enterotoxin C Detection. *Journal of Agricultural and Food Chemistry*, *71*(2), 1224-1233. https://doi.org/10.1021/acs.jafc.2c08147

Xue, S., Yin, L., Gao, S., Zhou, R., Zhang, Y., Jayan, H., El-Seedi, H. R., Zou, X., & Guo, Z. (2024). A film-like SERS aptasensor for sensitive detection of patulin based on GO@Au nanosheets. *Food Chemistry*, *441*, 138364. https://doi.org/10.1016/j.foodchem.2024.138364

Yang, M., Liu, G., Mehedi, H. M., Ouyang, Q., & Chen, Q. (2017). A universal SERS aptasensor based on DTNB labeled GNTs/Ag core-shell nanotriangle and CS-

Fe_3O_4 magnetic-bead trace detection of Aflatoxin B1. *Anal Chim Acta*, *986*, 122-130. https://doi.org/10.1016/j.aca.2017.07.016

Zhang, L., Liu, Y., Zhang, Q., Yao, W., Zhao, Z., Wang, X., Bao, Y., & Shi, W. (2024). Salvia miltiorrhiza polysaccharide mitigates AFB1-induced liver injury in rabbits. *Ecotoxicology and Environmental Safety*, *276*, 116344. https://doi.org/10.1016/j.ecoenv.2024.116344

Zhao, Y., Shao, J., Jin, Z., Zheng, W., Yao, J., & Ma, W. (2023). Plasmon-enhanced electroreduction activity of Au-AgPd Janus nanoparticles for ochratoxin a detection. *Food Chemistry*, *412*, 135526. https://doi.org/10.1016/j.foodchem.2023.135526

Zheng, F., Ke, W., Shi, L., Liu, H., & Zhao, Y. (2019). Plasmonic Au-Ag Janus Nanoparticle Engineered Ratiometric Surface-Enhanced Raman Scattering Aptasensor for Ochratoxin A Detection. *Analtical Chemistry*, *91*(18), 11812-11820. https://doi.org/10.1021/acs.analchem.9b02469

Figure Captions

Fig. 1. Schematic diagram of SERS aptasensor for AFB1 detection. Preparation of SiO_2@AgNPs-cDNA (A), and Au-Ag Janus NPs-apt (B), Detection of AFB1 (C).

Fig. 2. TEM images and physical appearances of SiO_2 (A) and SiO_2@AgNPs (B), TEM local enlarged image of SiO_2@AgNPs (C), XRD (D), FT-IR (E) spectra of SiO_2 and SiO_2@AgNPs, XPS spectra (F) of SiO_2@AgNPs, Changes in UV-Vis spectra during capture probe synthesis (G), ζ potential variations of AgNPs, SiO_2 and SiO2@AgNPs (H), SERS intensity of SiO_2^{MBA}, $AgNPs^{MBA}$ and SiO_2@$AgNPs^{MBA}$ (I).

Fig. 3. TEM images and physical appearances of AuNPs (A) and Au-Ag $Janus_{(2)}$ NPs (B), Size distribution of the Ag island of Au-Ag $Janus_{(2)}$ NPs (C), UV-vis spectra of AuNPs and Au-Ag Janus NPs (D), Zeta potential variations of Au-MBIA, Au-Ag $Janus_{(2)}$ NPs (E), Optimization of $AgNO_3$ addition (F), The SERS intensity of Au-Ag Janus NPs at 1280 cm^{-1} for 36 random points (G), The stability of Au-Ag Janus NPs under different pH (H), The stability of Au-Ag Janus NPs under different temperature and storage time (I).

Fig. 4. TEM image of aptasensor (A), TEM local enlarged image of SERS aptasensor (B), STEM elemental-mapping of SERS aptasensor, total elements iamge (C), Si (D(a)), O (D(b)), Ag (D(c)), Au (D(d)). Comparison of the UV-Vis spectra (E) and SERS intensity (F) of SiO_2@AgNPs, Au-Ag Janus NPs and SERS aptasensor, The stability of aptasensor under different pH, temperature and storage time (F).

Fig. 5. The SERS signal intensity at 1280 cm^{-1} of the aptasensor prepared with different volume ratios of capture probes and signal probes (A) and different incubation times

with 1 ng/mL AFB1 (B), The Raman spectra of the SERS aptasensor after incubation with different concentrations of AFB1 (C) and the linear relationship between the Lg C_{AFB1} and the SERS signal intensity of the aptasensor at 1280 cm^{-1} (D), specificity evaluation of aptasensor (E), The SERS intensity of aptasensor that incubated with 50 ng/mL AFB1 at 1280 cm^{-1} for 36 random points (F).

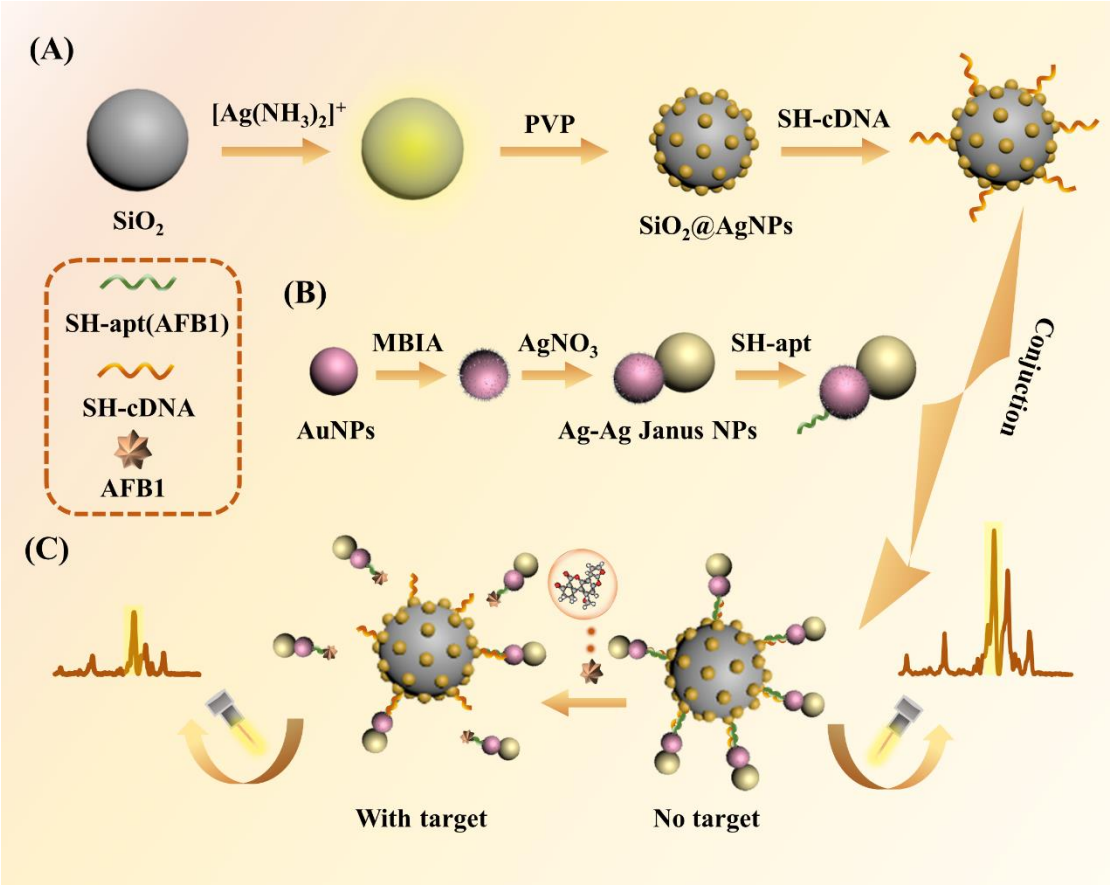

665

666 **Fig. 1.** Schematic diagram of SERS aptasensor for AFB1 detection. Preparation of

667 SiO2@AgNPs-cDNA (A), and Au-Ag Janus NPs-apt (B), Detection of AFB1 (C).

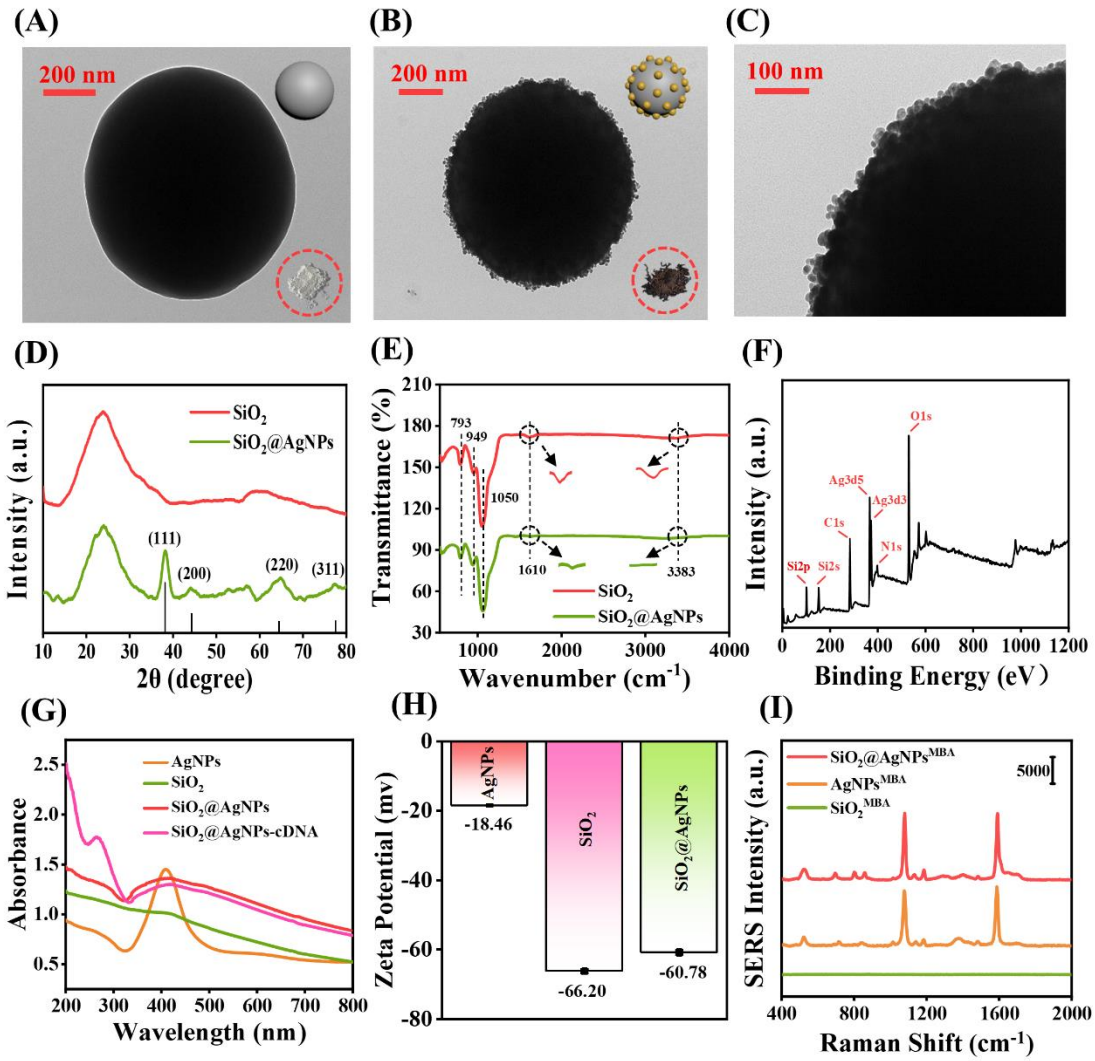

668

669 **Fig. 2.** TEM images and physical appearances of SiO_2 (A) and SiO_2@AgNPs (B), TEM

670 local enlarged image of SiO_2@AgNPs (C), XRD (D), FT-IR (E) spectra of SiO_2 and

671 SiO_2@AgNPs, XPS spectra (F) of SiO_2@AgNPs, Changes in UV-Vis spectra during

672 capture probe synthesis (G), ζ potential variations of AgNPs, SiO_2 and SiO2@AgNPs

673 (H), SERS intensity of SiO_2^{MBA}, $AgNPs^{MBA}$ and SiO_2@$AgNPs^{MBA}$ (I).

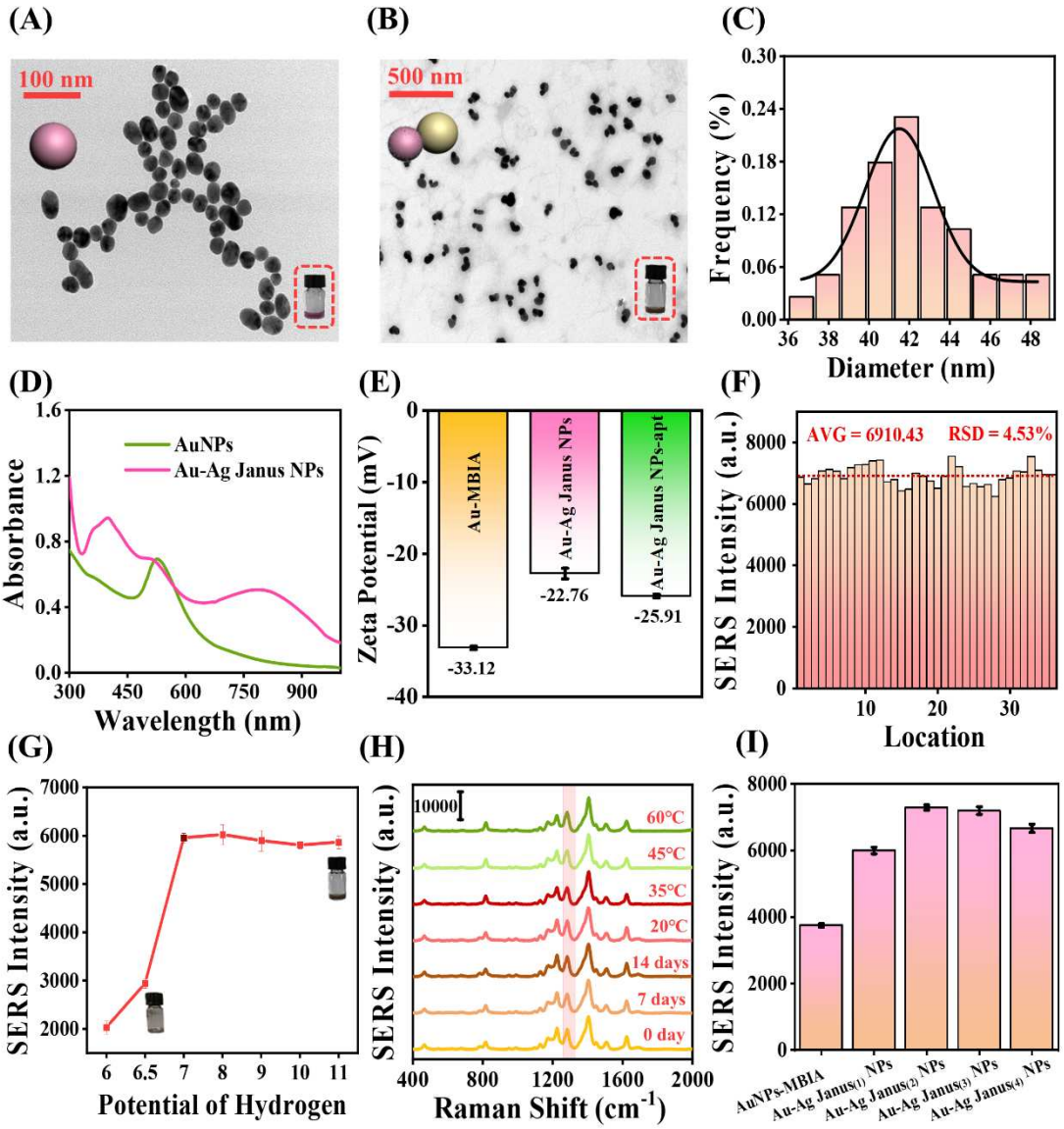

674

675 **Fig. 3.** TEM images and physical appearances of AuNPs (A) and Au-Ag Janus$_{(2)}$ NPs

676 (B), Size distribution of the Ag island of Au-Ag Janus$_{(2)}$ NPs (C), UV-vis spectra of

677 AuNPs and Au-Ag Janus NPs (D), Zeta potential variations of Au-MBIA, Au-Ag

678 Janus$_{(2)}$ NPs (E), The SERS intensity of Au-Ag Janus NPs at 1280 cm^{-1} for 36 random

679 points (F), The stability of Au-Ag Janus NPs under different pH (G), The stability of

680 Au-Ag Janus NPs under different temperature and storage time (H), Optimization of

681 $AgNO_3$ addition (I).

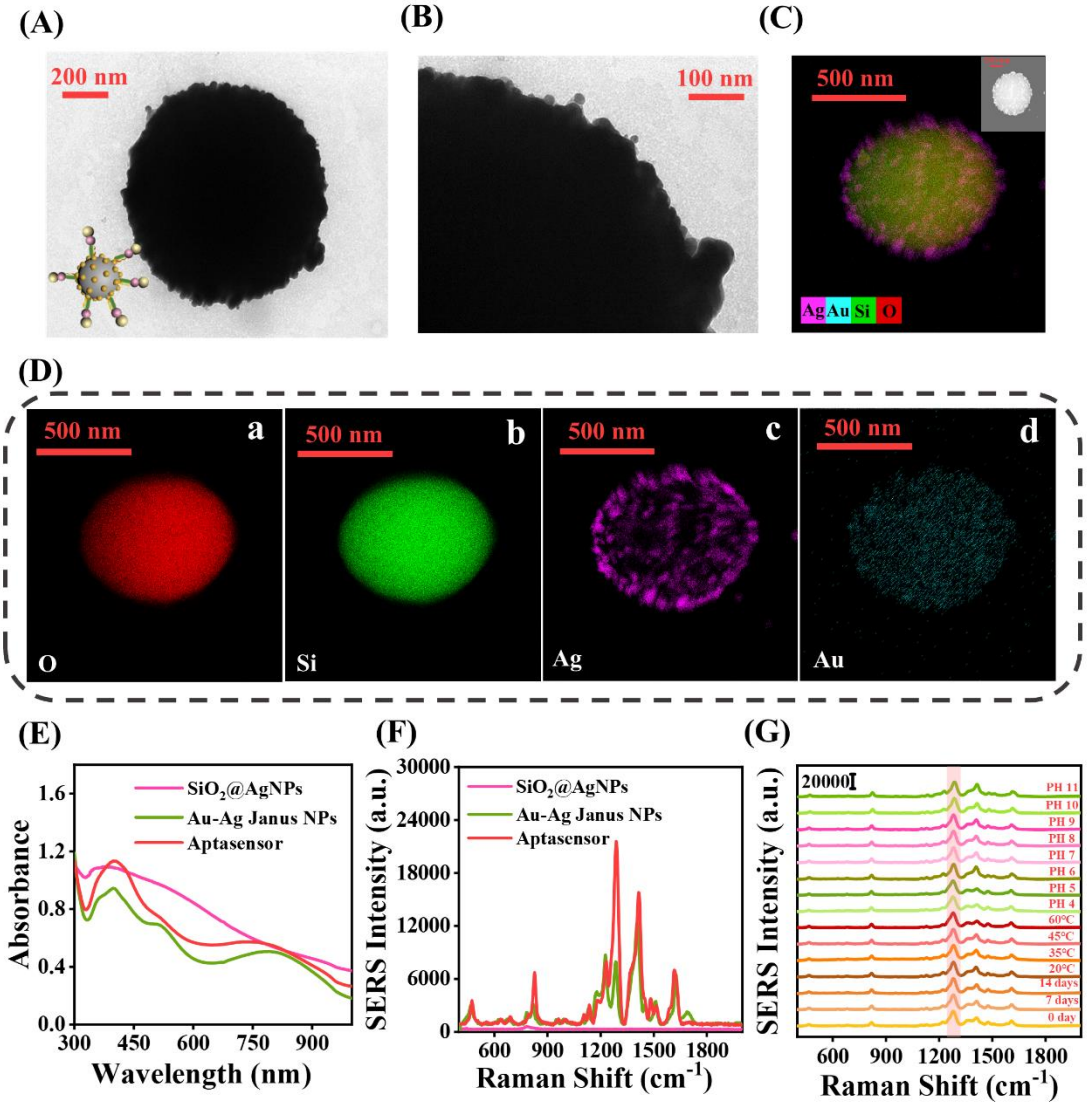

682

683 **Fig. 4.** TEM image of aptasensor (A), TEM local enlarged image of SERS aptasensor

684 (B), STEM elemental-mapping of SERS aptasensor, total elements iamge (C), Si (D(a)),

685 O (D(b)), Ag (D(c)), Au (D(d)). Comparison of the UV-Vis spectra (E) and SERS

686 intensity (F) of SiO2@AgNPs, Au-Ag Janus NPs and SERS aptasensor, The stability of

687 aptasensor under different pH, temperature and storage time (F).

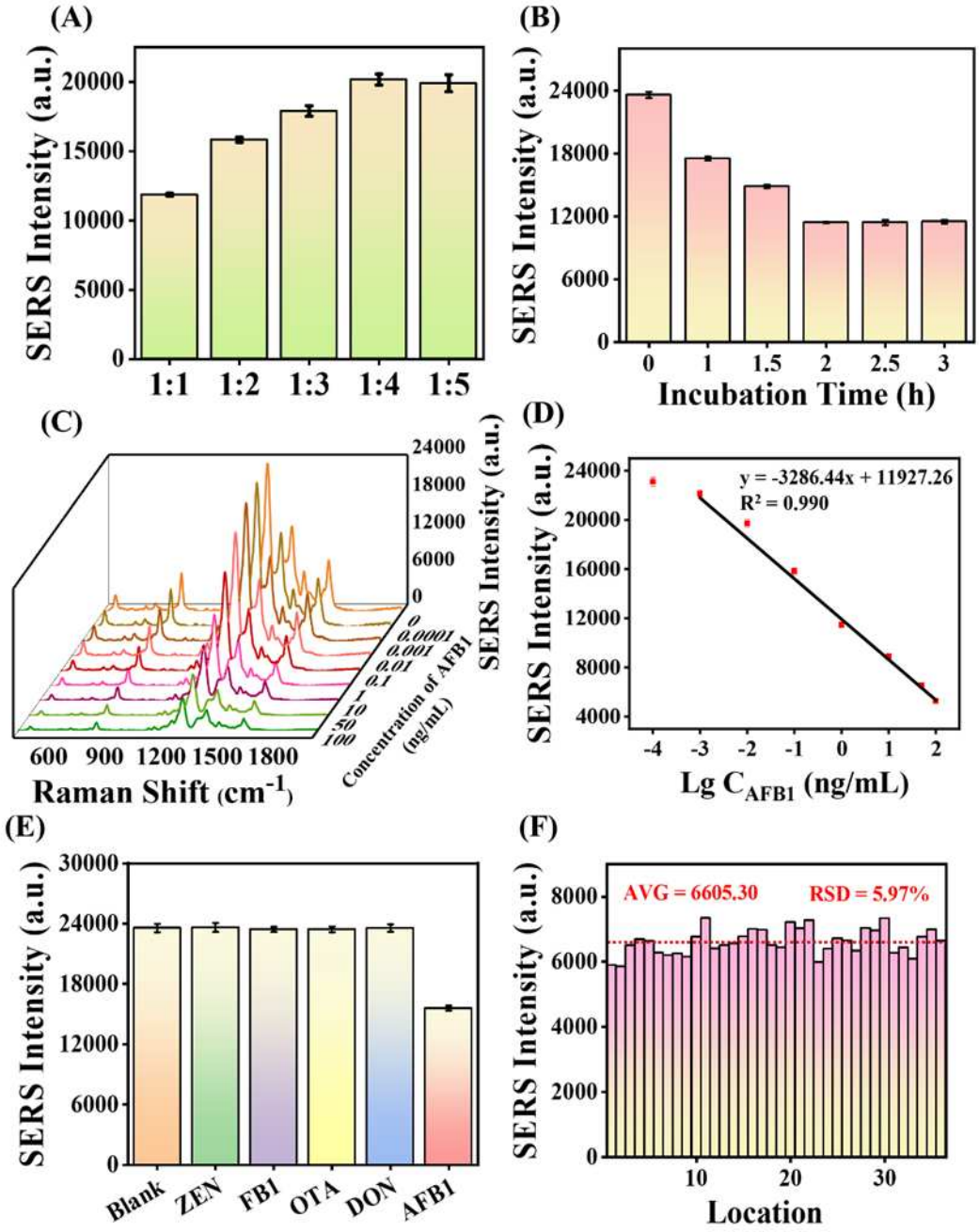

688

689 **Fig. 5.** The SERS signal intensity at 1280 cm^{-1} of the aptasensor prepared with different

690 volume ratios of capture probes and signal probes (A) and different incubation times

691 with 1 ng/mL AFB1 (B), The Raman spectra of the SERS aptasensor after incubation

692 with different concentrations of AFB1 (C) and the linear relationship between the Lg

693 C_{AFB1} and the SERS signal intensity of the aptasensor at 1280 cm^{-1} (D), specificity

694 evaluation of aptasensor (E), The SERS intensity of aptasensor that incubated with

695 50 ng/mL AFB1 at 1280 cm^{-1} for 36 random points (F).

Table Captions

Table 1. Comparison of different SERS detection methods for AFB1 (A), Detection results of AFB1 in maize samples by SERS aptasensor and HPLC methods (B).

Table 1

Comparison of different SERS detection methods for AFB1 (A), Detection results of AFB1 in maize samples by SERS aptasensor and HPLC methods (B).

	Linear detection range (ng/mL)	LOD (ng/mL)	Reference
(A) SERS method comparison	0.001-100	0.0006	(Wu et al., 2022)
	0.05-20	0.039	(Guo et al., 2024)
	0.1-5	0.03	(Jiao et al., 2025)
	0.01-10	0.00345	(Cao et al., 2024)
	0.001-100	0.0005	This Work

	Samples	Spiked (μg/kg)	SERS			HPLC	
			Detected (μg/kg)	Recovery (%)	RSD (%,n=5)	Detected (μg/kg）	Recovery (%)
(B) Maize samples detection	Naturally contaminated maize meal	/	6.209	108.94	1.56	5.699	/
		/	9.365	89.06	1.16	10.516	/
	Spiked maize meal	2.5	2.851	114.04	0.58	2.082	83.28
		7	6.209	88.70	1.00	7.884	112.629
	Spiked maize oil	1	0.923	92.30	1.15	0.957	95.70
		5	4.786	95.72	0.36	4.445	88.90